J. Fluid Mech. (2010), *vol.* 642, *pp.* 79–94.
doi:10.1017/S0022112009991753

The instability of a vortex ring impinging on a free surface

P. J. ARCHER, T. G. THOMAS† AND G. N. COLEMAN

Aerodynamics and Flight Mechanics Research Group, School of Engineering Sciences, University of Southampton, Southampton SO17 1BJ, UK

(Received 5 March 2009; revised 14 August 2009; accepted 14 August 2009; first published online 4 December 2009)

Direct numerical simulation is used to study the development of a single laminar vortex ring as it impinges on a free surface directly from below. We consider the limiting case in which the Froude number approaches zero and the surface can be modelled with a stress-free rigid and impermeable boundary. We find that as the ring expands in the radial direction close to the surface, the natural Tsai–Widnall–Moore–Saffman (TWMS) instability is superseded by the development of the Crow instability. The Crow instability is able to further amplify the residual perturbations left by the TWMS instability despite being of differing radial structure and alignment. This occurs through realignment of the instability structure and shedding of a portion of its outer vorticity profile. As a result, the dominant wavenumber of the Crow instability reflects that of the TWMS instability, and is dependent upon the initial slenderness ratio of the ring. At higher Reynolds number a short-wavelength instability develops on the long-wavelength Crow instability. The wavelength of the short waves is found to vary around the ring dependent on the local displacement of the long waves.

Key words: dynamics, instability, interactions

1. Introduction

Vortex rings are present in a wide range of engineering and biological flows (see Shariff & Leonard 1992). The interaction of a vortex ring with a free surface has been a topic of particular interest, as the flow experiences vortex tilting, stretching and reconnection, characteristic phenomena of fully turbulent flow. It has been shown that the instability of vortex pairs leads to the production of a series of vortex rings in both a stratified (Garten *et al.* 2001) and non-stratified (Crow 1970) ambient fluid; thus this investigation also models the surface interaction of submarine wakes generated during a diving procedure. Here we focus on the temporal development of a single ring as it approaches a surface directly from below, and consider how the growth of the ring instability is affected.

The behaviour of a ring as it approaches a clean (treated to remove surfactants) free surface directly from below was investigated experimentally by Song, Bernal & Tryggvason (1992). As the ring nears a depth d of order its radius R, its motion becomes increasingly influenced by its implied image above the surface. The ring stretches in the radial plane until, at a depth of order the core thickness δ, it expands

† Email address for correspondence: t.g.thomas@soton.ac.uk

laterally, approximately parallel to the surface, leading to a constriction of the core region. Three-dimensional disturbances develop around the ring, distorting the core region into a stationary wave. The wavy instability develops faster for rings at higher Reynolds number $Re = \Gamma/\nu$ (where Γ is the total circulation of the ring and ν is the kinematic viscosity of the fluid). When the ring expands to approximately four times its initial radius, the wavy core region connects at the surface in a series of U-shaped hoops. A number of numerical studies (Song *et al.* 1992; Wu, Fu & Ma 1995; Ye & Chu 1997) have been undertaken to investigate the interaction, however, their respective assumptions exclude the influence of the instability on the ring dynamics, which we seek to address in this study.

If the ring Froude number $Fr = \Gamma/\sqrt{gR^3}$ (where g is the gravitational acceleration) is small, the surface displacement caused by the ring is negligible and the behaviour of the ring is analogous to the head-on collision of two vortex rings, investigated experimentally by Lim & Nickels (1992) and numerically by Stanaway, Shariff & Hussain (1988). Here, the role of the virtual image is taken by the second ring. In the majority of the Lim and Nickels runs, for which the Reynolds number based on initial ring parameters $Re_p = UD/\nu \approx 1000$ (where U is the translational velocity of the ring and D is its diameter), the wavy instability developed simultaneously on both rings as they expanded. This culminates in multiple reconnections of the two core regions, forming a series of small rings. However, in certain runs, a much shorter wave instability, with wavelength of order of the core thickness was also present. The growth of both short- and long-wavelength instabilities has also been found in the temporal development of a vortex pair, studied experimentally by Leweke & Williamson (1998) and numerically by Laporte & Corjon (2000). Both studies found that regions of the two cores which are displaced close to one another by the long-wavelength instability are more susceptible to the short-wavelength instability. Unlike the symmetric long-wavelength instability, the short-wavelength instability grows 180° out of phase on each vortex pair.

Previously, examples of the short and long-wavelength instabilities have been recorded for vortex rings (see e.g. Krutzsch 1939; Maxworthy 1972; Widnall & Sullivan 1973) and a vortex pair (Crow 1970). A requirement for the amplification of both instabilities is the presence of a strain field, which is self-induced for the case of a vortex ring and originates from the neighbouring vortex filament in the case of a vortex pair. In the absence of strain, Kelvin (1880) showed that for a rectilinear vortex filament, disturbances in the form $\exp[\mathrm{i}(kz - \varpi t + m\theta)]$ (where k is axial wavenumber, ϖ is frequency and m is the wavenumber with respect to θ, the angular position around the core), rotate around the azimuth of the core without changing their shape. Widnall, Bliss & Tsai (1974) argued that in the presence of strain, helical waves with mode $m = \pm 1$ would be unstable if their rotation rate was equal to zero. This was later proved, in a more rigorous fashion, by Moore & Saffman (1975) and Tsai & Widnall (1976) for single line vortices and extended to Burgers and Lamb–Oseen vortices by Eloy & Le Dizés (1999). Vortex rings with a constant distribution of vorticity in the core region were also shown to be unstable to helical waves by Widnall & Tsai (1977). The instability is presently viewed as an example of an elliptic instability, for which a vortex with elliptic streamlines will undergo parametric resonance when two disturbance waves whose wavenumber m differs by 2, are simultaneously excited (see Kerswell 2002 for a review). For helical waves ($m \pm 1$) any number of radial modes can exist and are potentially unstable. The long-wavelength (hereafter Crow) instability is an example of the first radial mode. In effect, the disturbance is a sinusoidal displacement of the core in the

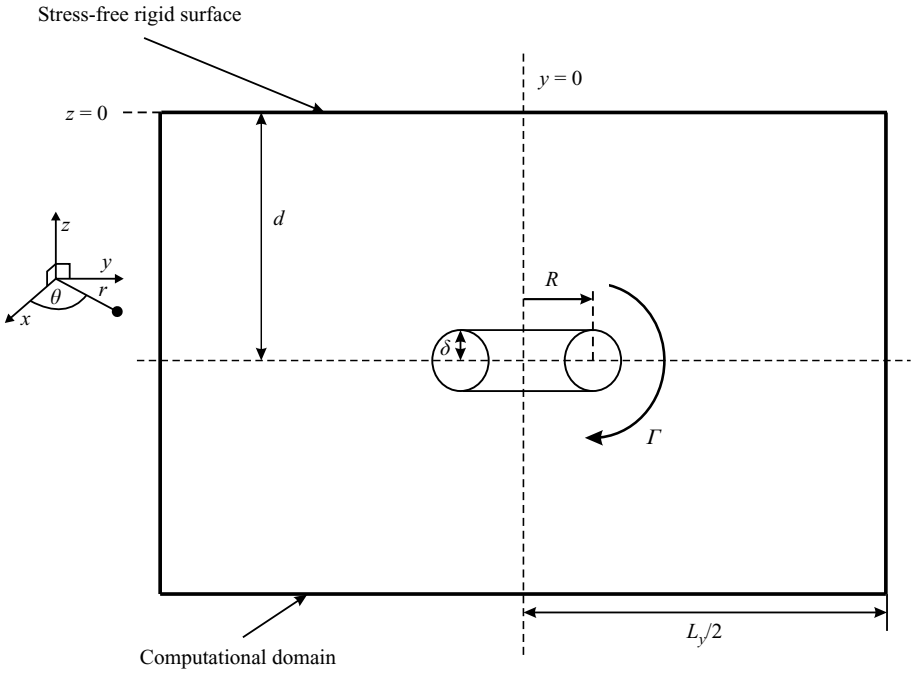

FIGURE 1. Schematic diagram of the head-on collision of a vortex ring with a surface.

plane of maximum amplification, otherwise known as a wave of pure bending. Crow (1970) showed that for the case of a vortex pair, the instability grew in a plane inclined at approximately 45° to the plane of symmetry separating the two cores. The short-wavelength or Tsai–Widnall–Moore–Saffman (hereafter TWMS) instability is an example of the second radial mode. It results in the inner and outer core regions moving in opposition to one another in a radial plane through the core centre, clearly visible in experimental visualizations of vortex rings (see e.g. figure 6 in Sullivan *et al.* 2008). For the case of rings and line vortices subjected to a plane strain, the first and second radial modes are most common as viscosity preferentially damps the higher order modes.

In this paper, we investigate the behaviour of a vortex ring as it approaches and interacts with a rigid free surface, considering the effect of Reynolds number on the ring structure, dynamics and instability growth. Our main aim is to understand how the different instability mechanisms can combine to produce the final ring structure.

2. Problem definition

We consider a single vortex ring of radius R and characteristic core radius δ, with circulation Γ and impulse $\boldsymbol{P}$. The non-dimensional parameters which define the investigation are the slenderness ratio $\epsilon = \delta/R$ of the ring, the Reynolds number $Re = \Gamma/\nu$ and Froude number $Fr = \Gamma/\sqrt{gR^3}$, where g is the acceleration due to gravity. We consider the limiting case in which $Fr \to 0$, allowing us to model the free surface with a stress-free rigid and impermeable boundary. The ring propagates vertically towards the free surface along the z direction with respect to Cartesian coordinates $\boldsymbol{x} = (x, y, z)$ as shown in figure 1. The vortex is initially embedded at depth d_0 such that it is centred about $\boldsymbol{x} = (0, 0, -d_0)$ at time $t = t_0$.

We measure the radius and depth of the ring by calculating the position of the centroid of enstrophy in the (r, z) plane,

$$R = \frac{1}{2\Omega} \int r|\omega|^2 \,\mathrm{d}x\,\mathrm{d}y\,\mathrm{d}z, \tag{2.1}$$

$$d = \left| \frac{1}{2\Omega} \int z|\omega|^2 \,\mathrm{d}x\,\mathrm{d}y\,\mathrm{d}z \right|, \tag{2.2}$$

where $\Omega = \int |\omega|^2 \mathrm{d}x\,\mathrm{d}y\,\mathrm{d}z$ is the total enstrophy, vorticity $\omega = \nabla \wedge \boldsymbol{u}$ with velocity components $\boldsymbol{u} = (u, v, w)$ and $r = \sqrt{x^2 + y^2}$.

3. Numerical approach

Our numerical approach is based on that used to investigate the evolution of unbounded vortex rings of differing slenderness ratio (Archer, Thomas & Coleman 2008). The incompressible Navier–Stokes equations are discretized on a conventional staggered grid using second-order finite differences in space and the Adams–Bashforth algorithm in time, with continuity imposed by applying pressure-correction methods with a parallel multigrid Poisson solver (Yao *et al.* 2001). The Cartesian computational domain assumes periodic boundary conditions in the x and y directions, so that we are, in effect, simulating an infinite array of vortices, but with the domain widths L_x and L_y chosen to be sufficiently large that the effects of periodicity are small (see Archer *et al.* 2008). We employ rigid (zero flux), free-slip boundary conditions at $z = 0$ and $z = -L_z$. By restraining the surface, we remove the influence of opposite-signed vorticity generated at the surface due to curvature (Longuet-Higgins 1998).

3.1. *Initial conditions*

The vortex ring is initiated with a Gaussian distribution of vorticity, which is positioned around a centreline path. The ring is perturbed from being perfectly circular by addition to the local radius of a set of Fourier modes of wavenumber 1 to 32, which have random phase and an amplitude of $0.0002R_0$. As the Gaussian distribution is only correct in the limit of $\delta \to 0$, the ring undergoes an initial adjustment during which it approaches its steady-state vorticity profile. To prevent the ring from impinging on the surface before it approximates a steady state would require that the ring be prescribed at a large depth below the surface. This would lead to an excessively large computation, since the domain must also be wide enough to allow the ring to expand upon reaching the surface. We solve the problem by evolving a ring in a smaller precursor simulation which not only allows the ring to adjust to its steady state but also develops the beginnings of structure around the ring as the TWMS instability develops. The precursor simulation assumes inflow and outflow boundary conditions in the direction of ring propagation and follows the same procedure described in Archer *et al.* (2008). A ring of radius R_{00} and circulation Γ_{00} is initialized with parameters $\delta_{00}/R_{00} = 0.2$, $Re_{00} = \Gamma_{00}/\nu = 7500$ and a radial profile proportional to $\exp(-(r/\delta_{00})^2)$. The cubic computational box is of size $8R_{00} \times 8R_{00} \times 8R_{00}$ with $256 \times 256 \times 256$ grid cells. After the ring has evolved for time $t_0\Gamma_{00}/(R_{00})^2 = 47$, the resultant vorticity field is used to prescribe the initial velocity field for the free-surface investigation. The domain is lengthened in the x and y directions by extending the vorticity field with extra cells of value zero. Similarly the domain is truncated above and below the ring in the z direction by removing cells. These procedures are acceptable because the vorticity field naturally goes to zero in both the lateral and longitudinal limits. The velocity field then follows by solving for

Case	R_0/R_{00}	Γ_0/Γ_{00}	δ_θ/R_0	a_1/R_0	a_e/R_0	Fr	Re
A	1.054	0.989	0.24	0.26	0.34	0	3708
B	1.054	0.989	0.24	0.26	0.34	0	7417
C	1.054	0.989	0.24	0.26	0.34	0	11126

TABLE 1. Run parameters. The single zero subscript refers to quantities at time t_0, corresponding to the start of the free-surface simulation. The double zero subscript refers to quantities at the start of the precursor simulation. See text for definition of δ_θ, a_1 and a_e.

the vector stream function that is consistent with the vorticity distribution, and taking its curl. The adjusted ring has radius R_0 and circulation Γ_0 and is embedded at depth $d_0 = 2.85R_0$ below the free surface at time t_0. Table 1 presents measures of the core radius δ_θ, a_1 and a_e at the start of the free-surface simulation. Here δ_θ is an integral measure of the core radius related to impulse by $\delta_\theta = 2(P/(\pi\Gamma) - (1/\Gamma \int r\omega_\theta \mathrm{d}r\mathrm{d}z)^2)$, where $P = \pi \int r^2\omega \mathrm{d}r\mathrm{d}z$ is the ring impulse and ω_θ is the azimuthal vorticity (Archer *et al.* 2008). More accessible from experimental data are the measures a_1 and a_e, which respectively refer to the distance from the core centre to the point of maximum tangential velocity and the speed-effective core radius. The speed-effective core radius a_e is defined as the core radius of a vortex ring propagating at an equivalent speed and with a uniform vorticity distribution, such that

$$U = \frac{\Gamma}{4\pi R}\left[\ln\left(\frac{8R}{a_e}\right) - 0.25\right], \tag{3.1}$$

where U is the propagation velocity (Lamb 1932). For the free-surface investigation, the computational domain initially measures $L_x = L_y = 13.3R_0$ and $L_z = 5.7R_0$ with $N_x = N_y = 448$ and $N_z = 192$ cells in the horizontal and vertical directions, respectively. Three thin-core cases are considered, identical except for Reynolds number (table 1). This will allow us to isolate the effect of viscosity on the behaviour of the ring instabilities.

3.2. *Interpolation and regridding of the computational domain*

The experiments of Song *et al.* (1992) show that the ring expands in the radial direction at the surface, leading to constriction of the core region. At the surface, δ can be approximated by the depth of the ring (see § 4.1). If circulation were conserved and the effect of viscosity ignored, one would expect the volume of the core region to be conserved and $\delta^2 \propto 1/R$. However, our findings show that δ decreases faster than the inviscid result (see figure 2*a*), which can be attributed to the decay of circulation from the ring (see § 4.1). The initial resolution of the laminar ring was shown to be sufficient by Archer *et al.* (2008) through comparison of results with a spectral code and monitoring of the rate of decay of kinetic energy against the rate of kinetic energy dissipation. However, to maintain adequate resolution of the core as the ring expands, it is necessary to interpolate the flowfield. This occurs in two discrete stages when the ring has expanded to $R = 1.2R_0$ and $R = 3.0R_0$. The initial interpolation doubles the number of grid cells in all directions and the second interpolation increases the resolution further by a factor of 1.5, preserving the number of grid points across the core (see figure 2*a*). The technique uses a Fourier scheme in the x and y directions and a bicubic method in the z direction, in which the gradient terms are evaluated through central differencing.

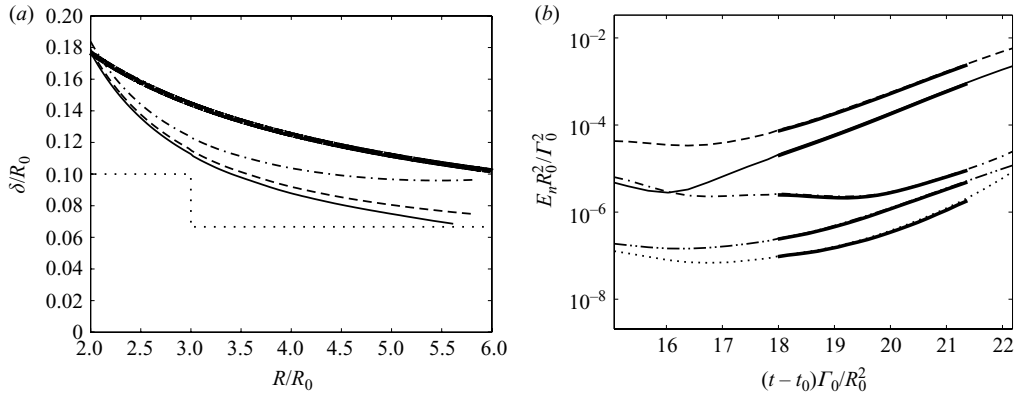

FIGURE 2. (*a*) Comparison of δ versus R for different Cases: – · – , A; – – – , B; — , C. The thick solid line denotes core radius predicted by conservation of the core volume. The dotted line indicates the minimum core radius above which the resolution quality exceeds that of the initial field. (*b*) Comparison of the evolution of energy of selected azimuthal modes for Case B and B′. Case B: – · · · – , $n=8$; – · – , $n=9$; – – – , $n=10$; — , $n=11$; ···· , $n=12$. Thick solid lines indicate corresponding results for Case B′.

To avoid excessively large computations it is necessary to truncate the domain in the z direction by removing cells from below the ring during the interpolation routine. However, the distance from the ring to the lower boundary is kept greater than $4d$ to prevent the image, associated with the zero-stress boundary condition at the bottom of the domain, from slowing the expansion of the ring at the surface. At the first interpolation, the z-axis is shortened to $L_z = 1.9R_0$ and then to $L_z = 1.27R_0$ at the second interpolation. A limit is also placed on the ring's radial expansion and the simulation is terminated before the ring moves within four ring depths of the lateral boundaries.

As the ring propagates towards the surface it produces a wake of weak vorticity (Archer *et al.* 2008). By truncating the domain we are removing a portion of this wake from the simulation. While this does not affect the dynamics of the ring, it will impact slightly on the integral measures of R, δ, Γ and d by introducing small discontinuities at $R/R_0 = 1.2$ and 3. Note, however, that the discontinuities at $R/R_0 = 3.0$ are too small to be discerned in the δ history shown in figure 2(*a*) (similar behaviour is observed at $R/R_0 = 1.2$). That the regridding of the domain has no adverse effects is demonstrated by examining the growth in energy of the ring's azimuthal modes, revealed by an azimuthal Fourier transform (see § 4.2), for a short time after the interpolation and truncation procedure. Figure 2(*b*) compares the evolution of selected modes for Cases B and B′. The cases are identical except that the domain for B′ is neither interpolated nor truncated at $(t - t_0)\Gamma_0/R_0^2 = 18$ (when $R/R_0 = 3$). There is no appreciable difference between the two cases.

4. Results

4.1. *Ring trajectory and circulation*

The interaction of the ring with the surface happens in three distinct phases: approach, slowing and expansion (figure 3). During the approach phase the ring is far enough from the surface for its motion to be unaffected by its image above the surface, and consequently it propagates by self-induction in approximately the same way

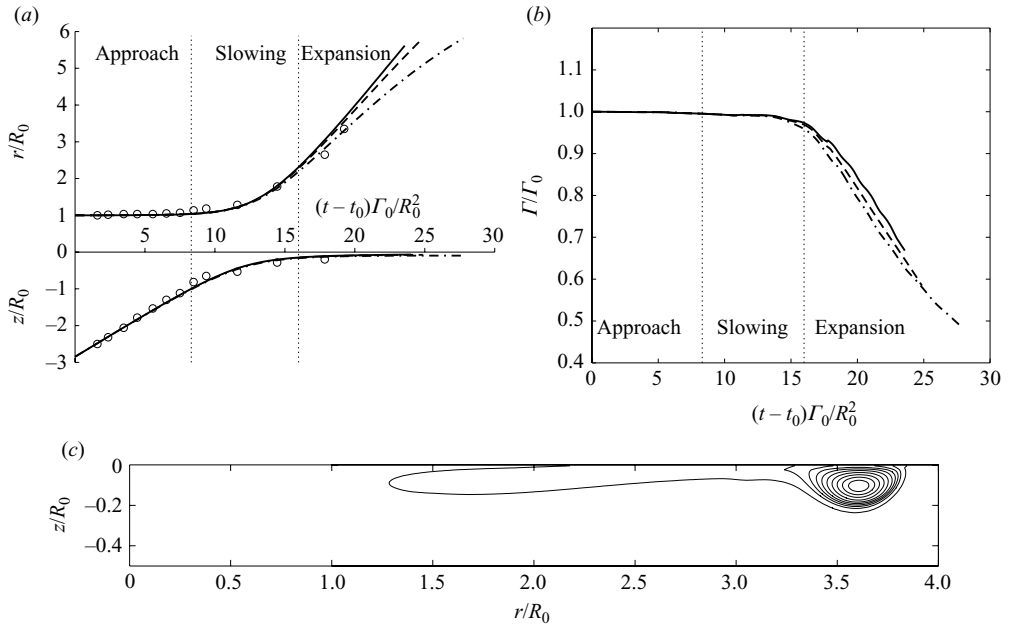

FIGURE 3. (*a*) Variation of the position of the ring's centroid of enstrophy in the z and r directions with time: – · – , Case A; – – – , Case B; — , Case C. (*b*) Time history of the overall circulation (same line styles used as in subfigure *a*). (*c*) Azimuthal vorticity ω_θ contours for Case B at time $(t-t_0)\Gamma_0/R_0^2 = 19.3$. (Contour increments of $1/10\omega_\theta^{max}$, minimum contour level at $2/100\omega_\theta^{max}$.)

as an unbounded ring. Figure 3(*a*) shows the depth and ring radius as a function of time for Cases A–C, as well as the experimental results of Song *et al.* (1992) (open symbols), for a more slender core ($a_e/R = 0.204$) at higher Reynolds number (15 100), and non-zero Froude number ($Fr = 0.287$). The experimental ring moves faster towards the surface than our cases because of its smaller slenderness ratio, which increases its translational velocity (3.1). During the approach phase the overall circulation is approximately constant (see figure 3*b*). As the depth of the ring below the surface becomes comparable to the radius it enters the slowing phase. Here, the influence of the virtual image above the surface becomes significant, reducing the ring's translational velocity and causing it to expand.

Finally, for $R \gtrsim 2.25R_0$, the ring enters the expansion phase, where it is strongly influenced by proximity to its image and its own curvature is less important. During this phase the ring and its image can be locally approximated by a pair of line vortices propagating parallel to the surface. Figure 3(*a*) shows that for Cases A–C the rate at which the ring expands depends on the Reynolds number Re, higher for greater Re. The velocity induced at a point by an infinite straight vortex filament is given by $V = \Gamma/2\pi h$, where h is the perpendicular distance from the point to the vortex filament. As the ring expands at a small distance from the surface the core radius is approximately equal to the ring depth (see figure 3*c*), thus the distance between the ring and its image h is approximately equal to twice the core radius, such that $V \propto 1/\delta$. Since the diffusion of the vortex core is smaller for the higher Reynolds cases (see figure 2*a*), the ring and its image are closer and correspondingly the ring propagates faster in the radial plane. Additionally, the circulation is also higher for the larger Reynolds number cases (see figure 3*b*), which also increases the rate at

which the rings expand, since $V \propto \Gamma$. During the expansion phase, the experimental results can be seen to diverge from Case C even though the Reynolds numbers are broadly similar. The divergence can be attributed to the experimental ring causing a displacement to the surface, absent from our stress-free rigid surface simulations. The surface displacement takes the form of a depression of depth approximately $0.02R_0$ (Song *et al.* 1992), which propagates ahead of the expanding ring. Surface curvature associated with the depression acts as a source of opposite-sign secondary vorticity ahead of the ring (Longuet-Higgins 1998) and reduces its circulation.

During the expansion phase we see a rapid approximately linear decay in circulation (see figure 3*b*) coinciding with the ring meeting its image at the surface. Vorticity contours show that the ring sheds a significant wake as it propagates under the surface (see figure 3*c*). However, this wake is not excluded from our calculation of the total circulation. Consequently we conclude that the decay of circulation can be attributed to the destruction of vorticity at the surface by the symmetry boundary condition. It results from the necessary condition that azimuthal vorticity ω_θ tends to zero at the surface, which annihilates the vorticity. Vorticity annihilation was also reported during simulations of the head-on collision of two vortex rings by Stanaway *et al.* (1988).

4.2. *Growth of unstable modes*

At time $t = t_0$, despite appearing to have smooth regular isosurfaces of vorticity, the ring already contains a very small amplitude wavy structure. The wavy structure was developed during the precursor simulation as a natural consequence of the ring's susceptibility to the TWMS instability. The relative strength of each wave component can be determined by calculating the perturbation kinetic energy E_n of azimuthal Fourier modes corresponding to n cycles around the ring (Archer *et al.* 2008). This is accomplished by interpolating the velocity field onto a cylindrical grid and performing a Fourier decomposition in the azimuthal direction. For a ring with a Gaussian distribution of vorticity, the theoretical estimate of the most amplified azimuthal mode $\widehat{n}$ is given by $\widehat{n} \approx 2.26/\epsilon$ (Shariff, Verzicco & Orlandi 1994). During the precursor simulation, $\widehat{n}$ lies in the range 11–9, tending to gradually smaller n as the core diffuses with time. This results in modes $n = 10$ and $n = 11$ being dominant at the start of the surface simulation (figure 4). As the ring propagates towards the surface, modes $n = 9$ and $n = 10$ amplify with the largest growth rate, consistent with the theoretical estimate. The growth of these two modes in the absence of a surface, obtained through a continuation of the precursor simulation is also shown in figure 4. The initially close fit between the simulations, shows that the surface has a negligible influence on the ring instability until the ring reaches the slowing phase.

During the slowing phase the ring radius increases, as the core radius decreases (see figure 2*a*), leading to a rapid decrease in slenderness ratio ϵ. Correspondingly, the window containing the most amplified mode $\widehat{n}$ increases and the modes previously amplified during the approach phase begin to decay, diverging from the unbounded results. Additionally, the self-induced strain responsible for amplification of the TWMS instability decreases as the ring expands. However, this is complemented by an increase in the strain contributed by its implied image as it nears the surface. This results in a change to the orientation of the strain field, which must rotate through approximately 90° in order to bridge between the two sources of strain.

As the radius of the ring increases, its curvature decreases and the ring and its image tend to approximate a pair of line vortices, which are known to be susceptible to the Crow instability (hereafter we use the term 'Crow' to refer to the instability

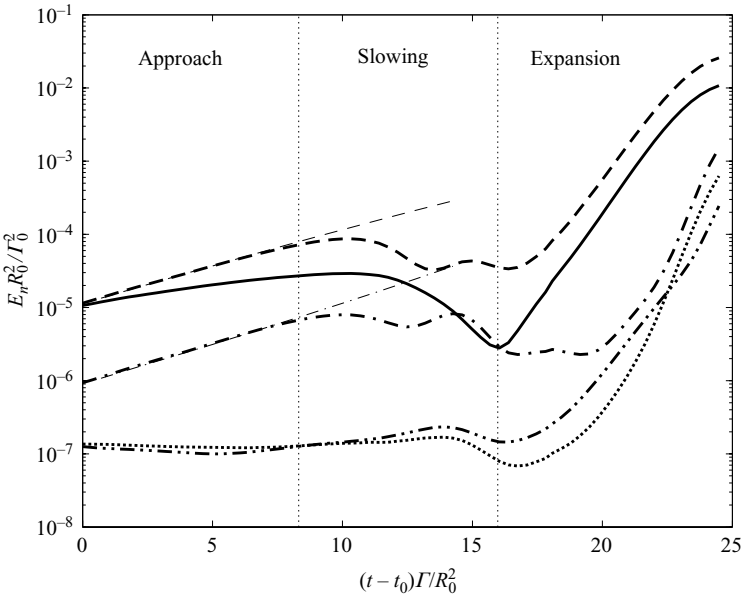

FIGURE 4. Evolution of the five initially most energetic azimuthal modes for Case B: – · · – , $n=8$; – · – , $n=9$; – – – , $n=10$; — , $n=11$; ····· , $n=12$. Also indicated, with corresponding thin line styles, are modes $n=9$ and 10, simulated within an unbounded domain (as in Archer *et al.* 2008).

of slightly curved vorticies close to the surface, implying a qualitative similarity to the strictly rectilinear case; for a formulation that accounts for curvature effects see Swearingen, Crouch & Handler 1995). Figure 4 shows that the azimuthal modes begin to amplify for a second time as the ring passes into the expansion phase. The close proximity of the ring to the surface results in the core radius being approximately half the distance between the ring and its image, i.e. equal to the distance to the surface. Leweke & Williamson (1998) showed that for a pair of line vortices characterized by $\delta/b=0.5$ (where b is the distance between the vortices), the minimum wavelength susceptible to the Crow instability is $\lambda_{min}=3.2b$ and the wavelength of maximum amplification is $\widehat{\lambda}=5b$. For Case B, at the start of the expansion phase this equates to a mode being unstable if $n<2\pi R/6.4\delta\approx 15$ and explains the broadband amplification of all of the modes in figure 4. The range of unstable azimuthal modes will increase monotonically with time as the core radius constricts and b decreases.

Since the azimuthal modes only decay during the slowing phase by approximately a decade before a second amplification begins, it appears that the wavy structure, initially developed by the TWMS instability, is further amplified by the Crow instability. The direct transfer of energy between helical modes of differing radial structures is unprecedented to our knowledge. To explain how this occurs, let us first consider the radial structure of the instability mechanisms. The TWMS instability is unstable to the second radial mode of helical waves ($m\pm1$), which feature one zero crossing in the radial plane through the core centre. This leads to the inner and outer core regions being displaced in opposite directions to one another in the plane of maximum strain (see figure 5*a*). In contrast, the Crow instability amplifies the first radial mode of helical waves ($m\pm1$), which have no zero crossings in the radial plane through the core centre. The inner and outer core are displaced in phase with one

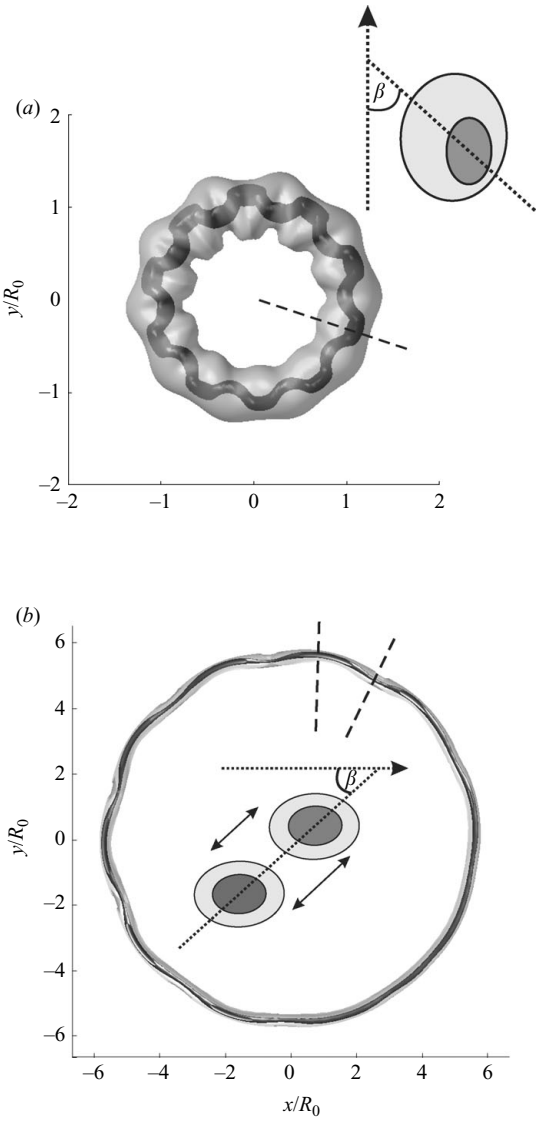

FIGURE 5. Illustration of the TWMS and Crow instabilities: (*a*) TWMS instability. Central figure taken from results used in Archer *et al.* (2008) for a ring with $\epsilon_0 = 0.2$ and $Re_0 = 7500$ at time $t\Gamma_0/R_0^2 = 80.95$, showing two isosurfaces of vorticity magnitude, $|\omega| R_0^2/\Gamma_0 = 3.5$ (dark) and $|\omega| R_0^2/\Gamma_0 = 1.0$ (light, translucent) indicating the inner and outer core respectively. Schematic diagram shows the displacement of the inner and outer core in the (r, z) plane marked with a dashed line. (*b*) Crow instability. Main figure shows the Crow instability of Case B at time $(t - t_0)\Gamma_0/R_0^2 = 24.2$, featuring two isosurfaces of vorticity magnitude, $|\omega| R_0^2/\Gamma_0 = 14.0$ (dark) and $|\omega| R_0^2/\Gamma_0 = 2.0$ (light, translucent) indicating the inner and outer core respectively. Schematics show the relative translation of the core region in the planes marked with dashed lines.

another in a wave of pure bending (see figure 5*b*). Since both instability mechanisms have the common feature of a stationary wave, it is feasible that transfer of energy from a TWMS to a Crow instability could occur if the outer core structure was either shed or reorganized to move back in phase with the inner core. However, this alone

is not a complete explanation, as the planes in which the two instabilities develop are approximately orthogonal to one another. The wavy structure developed by the TWMS instability must therefore rotate if it is to be further amplified by the Crow instability.

Prior to the expansion phase, the wavy structure is of very small scale, indistinguishable in isosurfaces of vorticity. However, an indication of the alignment of the wavy disturbances can be obtained by considering the distribution of the root mean square fluctuations of the azimuthal vorticity ω_θ^{rms} (figure 6*a*). Since ω_θ^{rms} is calculated by averaging in the azimuthal direction, it highlights deviations of ω_θ from its mean value around the ring (i.e. wavy behaviour). Contours of ω_θ^{rms} during the approach phase are shown in the lower subfigure of figure 6(*a*). The TWMS instability results in four distinct contoured regions, the inner two highly contoured regions correspond to the wavy displacement of the inner core and the lower outer contours correspond to the outer core. The outer contours are of smaller magnitude by virtue of the weaker ω_θ in the outer core. The plane in which the structure aligns is inclined at an angle $\beta = -60^\circ$ to the direction of ring propagation. Our method of measuring β differs from that used by Shariff *et al.* (1994) and Maxworthy (1972) who recorded angles of -48° and -45° respectively. In these papers the alignment of the wavy inner core was directly measured, however, this is not available to us during the approach phase due to the negligible amplitude of the wavy instability.

As the ring moves closer to the surface and begins to expand parallel to it, figure 6(*a*) shows that the contours of ω_θ^{rms} rotate by about 100°. As the wavy core is rotating, a region of vortical structure is deposited at the surface and remains there while the ring expands. The deposited structure is revealed in figure 6(*b*) by a low isosurface of the second invariant of the velocity gradient tensor. We infer that as the ring structure rotates near to the surface a portion of the outer core is stripped away from the ring. By shedding the outer core structure and rotating the inner core, the ring transfers its core structure from the second radial mode to the first, allowing further amplification of the wavy structure by the Crow instability. The deposited structure is also clearly visible in the experiments of the head-on collision of two vortex rings (see figures 1 and 3 of Lim & Nickels 1992, in which the deposited structure is labelled as a 'membrane'). For the head-on collision of a ring with a free surface, Song *et al.* (1992) used hydrogen bubbles to visualize the ring. Although this method of visualization does not make apparent regions of lower vorticity we would expect the same phenomena to be present there also.

The question arises as to whether the physical processes described above transfer energy between the orthogonal TWMS and Crow modes in a linear or nonlinear fashion. A nonlinear mechanism could readily explain the phenomena, however in this instance we note that the amplitude of the instability is still quite small when the energy is transferred. Instead, we believe that the modal transfer is achieved in a linear fashion involving slow changes in the mode shape as the ring approaches the surface. In effect there is coupling between nearby modes due to parametric changes (i.e. distance of the ring to the surface).

The rotation of the wavy structure and shedding of a portion of the outer core region occurs for all three cases. The cases do however vary in their respective growth rate α for both the TWMS and Crow instabilities. Viscosity is known to damp the TWMS instability (Shariff *et al.* 1994) leading to Case C having the highest instability growth rate on its approach to the surface. After the instability structure has rotated and is amplified once more by the Crow instability, Case C also initially features the highest growth rate for the dominant mode (figure 7). This is due to its higher

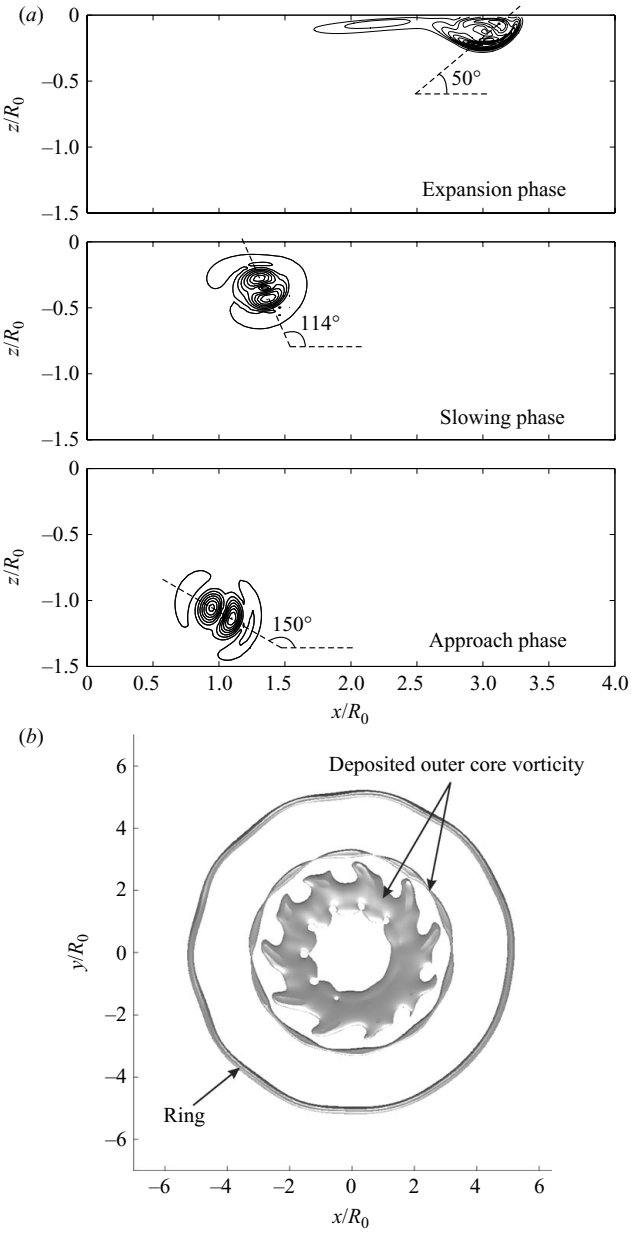

FIGURE 6. Evidence of modal transfer from the second to the first radial mode for Case B. (*a*) Rotation of the wavy inner core structure, visualized with contours of ω_θ^{rms} at times $(t-t_0)\Gamma_0/R_0^2 = 7.84, 12.47, 17.81$. (*b*) Evidence of the removal of a portion of the outer core vorticity, viewed with an isosurface of the second invariant of the velocity gradient tensor $\mathrm{II}R_0^4/\Gamma_0^2 = -0.005$, time $(t-t_0)\Gamma_0/R_0^2 = 23.0$.

circulation (figure 3*b*) and closer proximity to the surface (figure 2*a*), which increases the local strain on the core. The growth rate of the dominant mode for Cases B and C decays towards the end of their respective simulations as the modes begin to saturate (see $(t-t_0)\Gamma_0/R_0^2 > 23$ in figure 4).

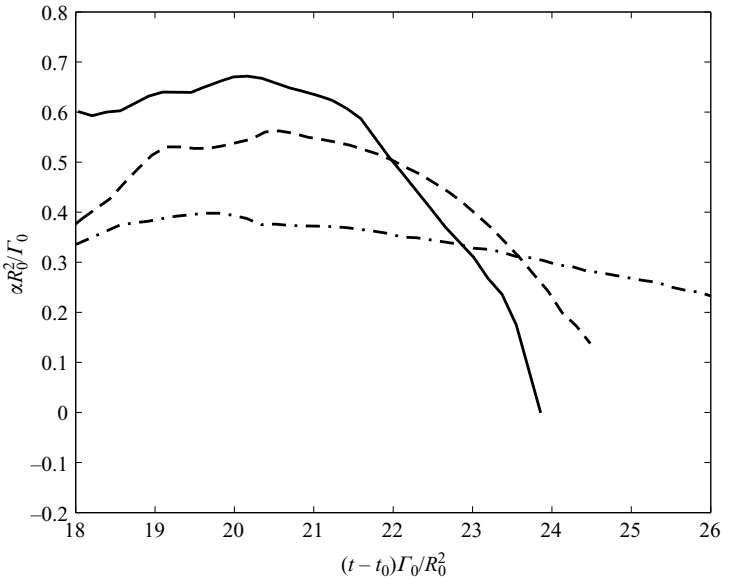

FIGURE 7. Variation of the growth rate for the dominant azimuthal mode during the expansion phase: – · – , Case A ($n=10$); – – – , Case B ($n=10$); — , Case C ($n=11$).

4.3. *The emergence of a short-wavelength instability*

In the latter stages of Case C an additional short-wavelength instability develops rapidly around the ring. Its wavelength is of order of the core thickness and its radial structure is suggested by the relative displacement of vorticity isosurfaces (see figure 8). The isosurfaces show that the inner core is displaced in opposition to the outer core, consistent with the amplification of helical waves ($m \pm 1$) of the second radial mode just as for the TWMS instability. Displacement of the inner and outer core is also apparent in the later stages of Case B. Case A, at the lowest Reynolds number, does not show any visible signs of a short-wavelength instability, which demonstrates the role of viscosity in damping the instability.

The development of the Crow instability is not uniform around the azimuth of the ring, an observation also made by Lim & Nickels (1992). This is due to constructive interference between neighbouring azimuthal modes. It is particularly apparent for Case C, in which the dominance of mode $n=11$ over $n=10$ is small, causing a noticeable 'lop-sidedness' in the growth of the long waves. This lop-sidedness leads to variation in the wavelength of the short waves around the ring. Where the core is displaced very close to the surface, by the Crow instability, the wavelength is significantly longer than at regions that are displaced farther from the surface. This is shown by the displacement of the weak outer core vorticity, marked with light grey in figure 8(*a*).

The superposition of short waves on a long-wavelength instability was also noted in the experiments of Lim & Nickels (1992) for colliding rings and by Leweke & Williamson (1998) for a pair of line vortices. However, the asymmetric development of the short-wavelength instability found by Leweke & Williamson (1998) is prevented here by the rigid surface, which enforces symmetry in the short waves with respect to their image. Leweke & Williamson (1998) found that the wavelength of their short-wave instability was approximately 80 % of the initial spacing between the vortex pairs. For our rings, the distance of the ring centroid to the surface and hence the

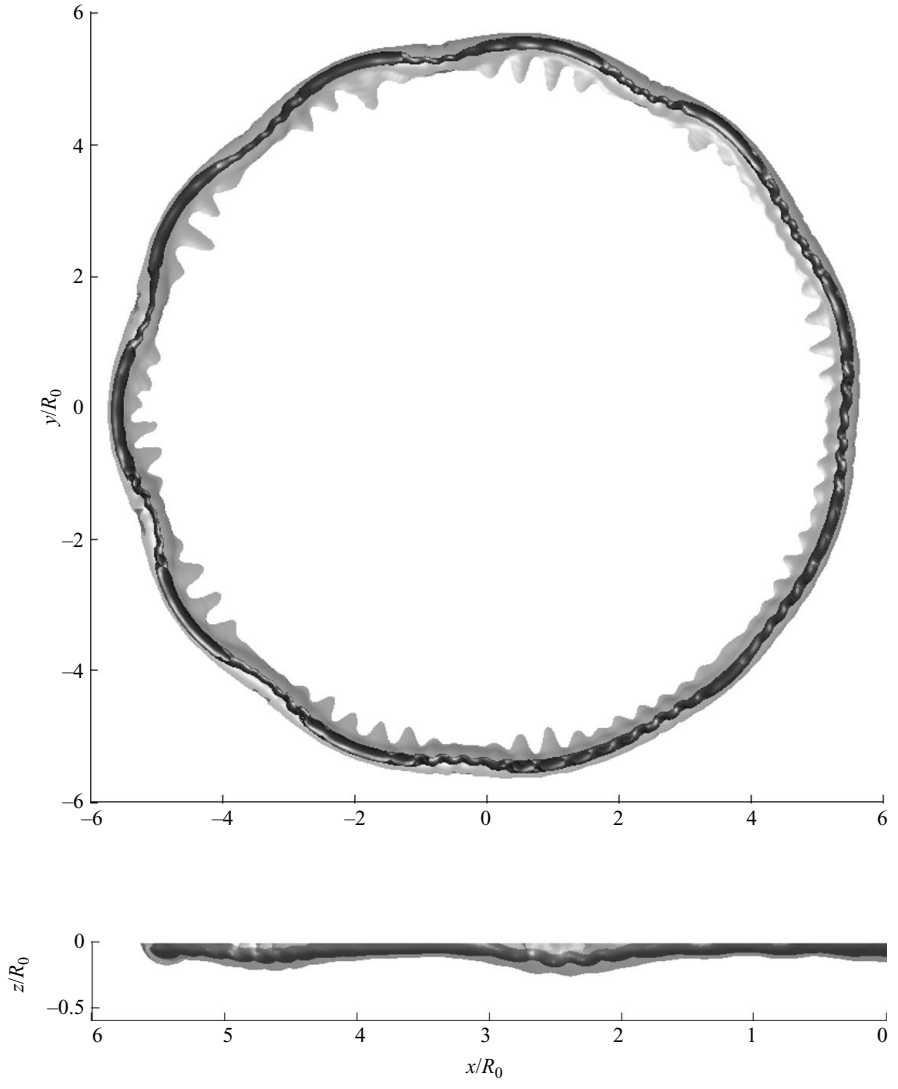

FIGURE 8. The emergence of a short-wavelength instability, superimposed on the Crow instability, for Case C at time $(t-t_0)\Gamma_0/R_0^2 = 23.24$, visualized with two isosurfaces of vorticity magnitude. Dark surface corresponds to $|\omega|\, R_0^2/\Gamma_0 = 16$ and light grey surface corresponds to $|\omega|\, R_0^2/\Gamma_0 = 1.25$. (*a*) View from above; (*b*) view from the side.

spacing from its image, decreases greatly as the ring expands, which does not allow direct comparison with their measure of λ_s.

5. Summary and closing comments

As a laminar vortex ring impinges on a rigid free surface its instability changes in both radial structure and alignment. Its approach to the surface is marked by the growth of the TWMS instability, which amplifies helical waves of the second radial mode. As the ring slows and then expands in the radial direction close to the surface, it is susceptible to the Crow instability, which amplifies helical waves

of the first radial mode. Despite being of differing radial structure and alignment, the evolution of the ring's azimuthal modal spectrum shows that the wavy structure developed by the TWMS instability acts as a perturbation to the Crow instability and is further amplified. The transfer of energy between the TWMS and Crow modes occurs through rotation of the wavy inner core structure and shedding of a portion of the outer core vorticity. The most unstable azimuthal modes amplified by the TWMS instability are given by $\widehat{n} \approx 2.26/\epsilon$ (Shariff *et al.* 1994). Thus the initial slenderness ratio ϵ determines the number of cycles of the long wave amplified by the Crow instability and the final ring structure. The close agreement between our findings and the experimental observations of a ring impinging on a deformable surface (Song *et al.* 1992) and the head-on collision of two rings (Lim & Nickels 1992), suggests that the same mechanisms are at play there as well.

During the latter stages of our moderate and high Reynolds number cases a short-wavelength instability grows, superimposed on the long waves that are amplified by the Crow instability. The displacement of the inner and outer core regions suggests that the instability amplifies helical waves of the second radial mode, just as for the TWMS instability. The wavelength of the short waves is modulated around the ring and is greatest in regions of the core that are displaced closest to the surface by the Crow instability. Despite forming a number of seemingly identical rings, Lim & Nickels (1992) found that the short-wavelength instability did not develop in all runs. Although we find that the short-wavelength instability grows faster than the Crow instability, its appearance will depend on the relative growth of the earlier TWMS instability. If the Crow instability is sufficiently perturbed before the expansion phase, the long waves will be sufficiently developed to pinch off to form rings prior to the appearance of the short waves.

The formation of U-shaped loops, associated with the disconnection of the vortex core around the ring and reconnection with its image above the surface, is absent from our simulations, in contrast to the experiments of Song *et al.* (1992). However, we do find a large-amplitude long-wavelength displacement of the core, due to the Crow instability. This occurs in the experiments, immediately prior to the reconnection process (see figure 1*d* in Lim & Nickels 1992). It is likely therefore that a larger computational domain would capture this phenomena. As described above, we can estimate the slenderness ratio of the experimental rings from the number of long waves that develop around the ring as it expands. Note that Song *et al.* (1992) and Lim & Nickels (1992) considered slightly thinner rings, with $0.12 \lesssim \epsilon \lesssim 0.16$. Our results suggest that the radius at which the ring disconnects and reconnects with its image (or neighbour) is likely to be a function of the slenderness ratio ϵ, the initial depth d_0 and the Reynolds number. Decreasing ϵ or increasing the Reynolds number raises the growth rate of both the TWMS and Crow instabilities. Also, by increasing d_0, the TWMS instability would have been more developed when the ring reached the surface, requiring less amplification by the Crow instability. However, if either of the above parameters were sufficiently modified, the ring may transition to turbulence prior to interacting with the surface. Future work will consider these factors, as well as the influence of a deforming free surface.

This research was supported by the UK Engineering and Physical Sciences Research Council (EPSRC) through a Platform grant on turbulence (Grant GR/582947/01). The work was done as part of the UK Turbulence Consortium, using the facilities of HPCx (Grant EP/D044073/1). Special thanks go to Dr J. A. Redford, Shankar Balakrishnan and Dr K. Shariff for their support, encouragement and expertise.

REFERENCES

Archer, P. J., Thomas, T. G. & Coleman, G. N. 2008 Direct numerical simulation of vortex ring evolution from the laminar to the early turbulent regime. *J. Fluid Mech.* **598**, 201–226.

Crow, S. C. 1970 Stability theory for a pair of trailing vortices. *AAIA* **8**, 2172–2179.

Eloy, C. & Le Dizés, S. 1999 Three-dimensional instability of burgers and Lamb–Oseen vortices in a strain field. *J. Fluid Mech.* **378**, 145–166.

Garten, J. F., Werne, J., Fritts, D. C. & Arendt, S. 2001 Direct numerical simulations of the crow instability and subsequent vortex reconnection in a stratified fluid. *J. Fluid Mech.* **426**, 1–45.

Kelvin, Lord 1880 On the vibrations of a columnar vortex. *Phil. Mag.* **10**, 155–168.

Kerswell, R. R. 2002 Elliptical instability. *Annu. Rev. Fluid Mech.* **34**, 83–113.

Krutzsch, C. H. 1939 Über eine experimentell beobachtete erscheining an werbelringen bei ehrer translatorischen beivegung in weklechin, flussigheiter. *Ann. Phys.* **5**, 497–523.

Lamb, H. 1932 *Hydrodynamics*, 6th edn. Dover.

Laporte, F. & Corjon, A. 2000 Direct numerical simulations of the elliptic instability of a vortex pair. *Phys. Fluids* **12**, 1016–1031.

Leweke, T. & Williamson, C. H. K. 1998 Cooperative elliptic instability of a vortex pair. *J. Fluid Mech.* **360**, 85–119.

Lim, T. T. & Nickels, T. B. 1992 Instability and reconnection in the head-on collision of two vortex rings. *Nature* **357**, 225–227.

Longuet-Higgins, M. S. 1998 Vorticity and curvature at a free surface. *J. Fluid Mech.* **356**, 149–153.

Maxworthy, T. 1972 The structure and stability of vortex rings. *J. Fluid Mech.* **51**, 15–32.

Moore, D. W. & Saffman, P. G. 1975 The instability of a straight vortex filament in a strain field. *Proc. R. Soc. Lond.* **346**, 415–425.

Shariff, K. & Leonard, A. 1992 Vortex rings. *Annu. Rev. Fluid Mech.* **24**, 235–279.

Shariff, K., Verzicco, R. & Orlandi, P. 1994 A numerical study of three-dimensional vortex ring instabilities: viscous corrections and early nonlinear stage. *J. Fluid Mech.* **279**, 351–375.

Song, M., Bernal, L. P. & Tryggvason, G. 1992 Head-on collision of a large vortex ring with a free surface. *Phys. Fluids* A **4**, 1457–1466.

Stanaway, S., Shariff, K. & Hussain, F. 1988 Head-on collision of viscous vortex rings. *Proc. 1988 Summer Program* pp. 287–309.

Sullivan, I. S., Niemela, J. J., Hershberger, R. E., Bolster, D. & Donnelly, R. J. 2008 Dynamics of thin vortex rings. *J. Fluid Mech.* **609**, 319–347.

Swearingen, J. D., Crouch, J. D. & Handler, R. A. 1995 Dynamics and stability of a vortex ring impacting a solid boundary. *J. Fluid Mech.* **297**, 1–28.

Tsai, C.-Y. & Widnall, S. E. 1976 The stability of short waves on a straight vortex filament in a weak externally imposed strain field. *J. Fluid Mech.* **73**, 721–733.

Widnall, S. E., Bliss, D. B. & Tsai, C.-Y. 1974 The instability of short waves on a vortex ring. *J. Fluid Mech.* **66**, 35–47.

Widnall, S. E. & Sullivan, J. P. 1973 On the stability of vortex rings. *Proc. R. Soc. London.* A **332**, 335–353.

Widnall, S. E. & Tsai, C.-Y. 1977 The instability of the thin vortex ring of constant vorticity. *Phil. Trans. R. Soc. Lond.* **287**, 273–305.

Wu, C., Fu, Q. & Ma, H. 1995 Interactions of three-dimensional viscous axisymmetric vortex rings with a free surface. *Acta Mech. Sin.* **11**, 229–238.

Yao, Y. F., Thomas, T. G., Sandham, N. D. & Williams, J. J. R. 2001 Direct numerical simulation of turbulent flow over a rectangular trailing edge. *Theor. Comput. Fluid Dyn.* **14**, 337–358.

Ye, Q. & Chu, C. K. 1997 The nonlinear interaction of vortex rings with a free surface. *Acta Mech. Sin.* **13**, 120–129.